Molecular mechanisms of cutis laxa– and distal renal tubular acidosis–causing mutations in V-ATPase *a* subunits, ATP6V0A2 and ATP6V0A4

Received for publication, September 20, 2017, and in revised form, December 20, 2017 Published, Papers in Press, January 8, 2018, DOI 10.1074/jbc.M117.818872

Sally Esmail[‡1], Norbert Kartner[‡], Yeqi Yao[‡], Joo Wan Kim[‡2], Reinhart A. F. Reithmeier[§], and Morris F. Manolson[‡§3]

From the [‡]Dental Research Institute, Faculty of Dentistry, University of Toronto, Toronto, Ontario M5G 1G6 and the [§]Department of Biochemistry, University of Toronto, Toronto, Ontario M5S 1A8, Canada

Edited by Peter Cresswell

The *a* subunit is the largest of 15 different subunits that make up the vacuolar H^+-ATPase (V-ATPase) complex, where it functions in proton translocation. In mammals, this subunit has four paralogous isoforms, *a*1–*a*4, which may encode signals for targeting assembled V-ATPases to specific intracellular locations. Despite the functional importance of the *a* subunit, its structure remains controversial. By studying molecular mechanisms of human disease– causing missense mutations within *a* subunit isoforms, we may identify domains critical for V-ATPase targeting, activity and/or regulation. cDNA-encoded FLAG-tagged human wildtype ATP6V0A2 (*a*2) and ATP6V0A4 (*a*4) subunits and their mutants, $a2^{P405L}$ (causing cutis laxa), and $a4^{R449H}$ and $a4^{G820R}$ (causing renal tubular acidosis, dRTA), were transiently expressed in HEK 293 cells. *N*-Glycosylation was assessed using endoglycosidases, revealing that $a2^{P405L}$, $a4^{R449H}$, and $a4^{G820R}$ were fully *N*-glycosylated. Cycloheximide (CHX) chase assays revealed that $a2^{P405L}$ and $a4^{R449H}$ were unstable relative to wildtype. $a4^{R449H}$ was degraded predominantly in the proteasomal pathway, whereas $a2^{P405L}$ was degraded in both proteasomal and lysosomal pathways. Immunofluorescence studies disclosed retention in the endoplasmic reticulum and defective cell-surface expression of $a4^{R449H}$ and defective Golgi trafficking of $a2^{P405L}$. Co-immunoprecipitation studies revealed an increase in association of $a4^{R449H}$ with the V_0 assembly factor VMA21, and a reduced association with the V_1 sector subunit, ATP6V1B1 (B1). For $a4^{G820R}$, where stability, degradation, and trafficking were relatively unaffected, 3D molecular modeling suggested that the mutation causes dRTA by blocking the proton pathway. This study provides critical information that may assist rational drug design to manage dRTA and cutis laxa.

Vacuolar H^+-ATPases (V-ATPases)[4] are conserved, multisubunit rotary proton pumps that play crucial roles in regulating the pH of cells and their intracellular compartments (1–5). They can be categorized as endomembrane or plasma membrane V-ATPases, based on their subcellular localization (6, 7). Endomembrane V-ATPases are expressed in all eukaryotic cells in the membranes of acidic organelles like lysosomes, endosomes, and the Golgi apparatus, where they translocate protons to acidify the luminal compartments of the organelles (8). Plasma membrane V-ATPases traffic to the surfaces of some specialized cells, such as osteoclasts, kidney-intercalated cells, and metastatic cancer cells, where they secrete protons into the extracellular fluid (6, 9–11).

The V-ATPase complex consists of 15 different subunits arranged into two major sectors, the cytoplasmic V_1 sector and the membrane-integrated V_0 sector. V_1 is responsible for ATP hydrolysis that provides the energy to rotate a central shaft that powers proton translocation (3). V_0 contains a coupled rotor that carries protons for transport through a proton channel pathway formed largely by the approximately 100-kDa *a* subunit (2, 12). The *a* subunit is the largest V-ATPase subunit, and in mammals there are four isoforms, *a*1–*a*4. The N-terminal half of the protein (NT*a*) is hydrophilic and associates with subunits of the V_1 sector in the V-ATPase complex, and the C-terminal half (CT*a*) is an integral membrane domain consisting of 8 transmembrane α-helices (TMs) and a cytoplasmic (C-terminal) tail domain (CTD). Whereas *a*1 and *a*2-containing V-ATPase complexes are targeted to endomembranes, *a*3 and *a*4 complexes are targeted to plasma membranes in some specialized cells (13, 14).

Human missense mutations of the *a* subunits are implicated in diverse diseases (1, 15). For example, mutations affecting the function of *a*2 result in cutis laxa (wrinkled skin syndrome), where aberrant Golgi function results in glycosylation defects with consequent abnormal elastin processing

This work was supported in part by the Canadian Institutes of Health Research Grants MOP-12333 and PJT-148508 (to M. F. M.). The authors declare that they have no conflicts of interest with the contents of this article.

[S] This article contains Tables S1 and S2.

[1] Supported in part by a scholarship from the Toronto Musculoskeletal Centre.

[2] Supported by a scholarship from the Canadian Institutes of Health Research/Institute of Musculoskeletal Health and Arthritis.

[3] To whom correspondence should be addressed: Faculty of Dentistry, University of Toronto, 124 Edward St., Toronto, Ontario M5G 1G6, Canada. Tel.: 416-864-8234; Fax: 416-979-4936; E-mail: m.manolson@utoronto.ca.

[4] The abbreviations used are: V-ATPase, vacuolar-type H^+-ATPase; CFTR, cystic fibrosis transmembrane-conductance regulator; CHX, cycloheximide; CT*a*, C-terminal (integral membrane) half of V-ATPase *a* subunit; CTD, C-terminal (cytoplasmic) tail domain (of V-ATPase *a* subunit); dRTA, distal renal tubular acidosis; Endo H, endo-β-N-acetylglucosaminidase H; ER, endoplasmic reticulum; NT*a*, N-terminal (cytoplasmic) half of V-ATPase *a* subunit; PNGase F, peptide:*N*-glycosidase F; TM, transmembrane α-helix; DMEM, Dulbecco's modified Eagle's medium; DPBS, Dulbecco's phosphate-buffered saline; HRP, horseradish peroxidase; GAPDH, glyceraldehyde-3-phosphate dehydrogenase; HA, hemagglutinin.

that affects skin and internal organs (16–18). Mutations that affect *a*3 function result in inability of osteoclasts to resorb bone, causing autosomal malignant osteopetrosis that is characterized by dense, brittle bone (19, 20). Loss of *a*4 function due to mutation results in distal renal tubular acidosis (dRTA) with occasional hearing loss (21, 22). Here we focus on the effect of human mutations on *a*2 traffic to Golgi and *a*4 traffic to the plasma membrane based on their proposed *in vivo* locations and functions.

Despite such important implications for *a* subunit functions in disease, the structures of human *a* subunit isoforms are still controversial because of a lack of high-resolution structural data. Recently, however, a 6.4-Å model of the membrane-integrated domain of the yeast *a* subunit (Vph1p) has been published (23, 24). This model is based on a synthesis of data derived from cryo-EM 3D reconstruction, evolutionary covariance mapping of key residues, and low resolution X-ray crystallography. It confirms that the *a* subunit membrane domain consists of 8 TMs, as has been previously shown (2, 12), with TM7 and TM8 highly tilted and forming an interface with the V_0 rotor *c*-ring that enables proton translocation at the *a* subunit/*c*-ring interface.

Despite such recent advances, knowledge of *a* subunit folding, targeting, and assembly into the V-ATPase holocomplex remains sparse. Considerably more investigation will be required to elucidate issues such as, for example, the mechanism of plasma membrane *a* subunit targeting, the resolution of which will be required before efforts at designing strategies for targeted therapeutic interventions can realistically be considered. To that end, we conjectured that human disease–causing missense mutations within *a* subunits could be used to identify critical domains essential for V-ATPase targeting, activity and/or regulation. As an approach to testing this, we have studied the molecular consequences of introducing the cutis laxa–causing mutation, Pro-405 → Leu (P405L) in *a2*, and the dRTA-causing mutations, Arg-449 → His (R449H) and Gly-820 → Arg (G820R) in *a4*, into epitope-tagged human *a* subunit constructs for expression and characterization in the HEK 293 mammalian expression system. We present here results of these studies with respect to subunit glycosylation, stability, degradation, incorporation into V-ATPase complexes, and subcellular localization.

Results

Amino acid residues a2 Pro-405, a4 Arg-449, and a4 Gly-820 are highly conserved

Alignments of *a* subunit polypeptide sequence segments affected by the human mutations causing cutis laxa and dRTA that are under study in the present work are shown in Fig. 1, *A* and *B*. The mutated residues (highlighted in *red*) are identical in all four human and mouse *a* subunit isoforms, and also in the yeast *a* subunit isoform, Vph1p (highlighted in *yellow*). Fig. 1*A* shows a segment of the integral membrane domain of the *a* subunit, where human mutations in *a2* Pro-405 (in TM1; TMs highlighted in *blue*) and *a4* Arg-449 (in TM3) result in cutis laxa and dRTA, respectively. Fig. 1*B* shows alignments for a C-terminal segment of the *a* subunit comprising the CTD, where the human mutation in *a*4 Gly-820 results in dRTA. Thus, the three mutations under consideration here, $a2^{P405L}$, $a4^{R449H}$, and $a4^{G820R}$, all affect highly conserved amino acid residues.

Glycosylation and stability of cutis laxa mutant, $a2^{P405L}$

We have previously shown that all human *a* subunit isoforms are *N*-glycosylated and that *N*-glycosylation is required for their stability (25, 26). We have also shown in previous work that in the case of the osteopetrosis mutation, $a3^{R444L}$, the *a* subunit is misfolded, unglycosylated, retained in the ER, and ultimately subjected to proteolytic degradation (20). It was of interest, therefore, to determine whether the cutis laxa and dRTA mutations have similar impacts on *a*2 and *a*4 subunits, respectively, using methods for assessing *N*-glycosylation and stability that were previously described (25). Briefly, glycosylation and stability were tested in HEK 293 cells by transient transfection and expression of FLAG-tagged wildtype and mutation-bearing *a*2 and *a*4 subunit constructs. Whole-cell lysates prepared 24 h post-transfection were treated with peptide *N*-glycosidase F (PNGase F) to assess whether mutant proteins, $a2^{P405L}$, $a4^{R449H}$, and $a4^{G820R}$, were *N*-glycosylated, and with endo-β-*N*-acetylglucosaminidase H (Endo H) to determine whether any bound glycans were of the high mannose or hybrid type (27, 28). Stability was assessed using the CHX chase method as previously described (25, 26). Briefly, cells were treated, 24 h post-transfection, with CHX (10 μg/ml) for up to 12 h, and whole-cell lysates were prepared, immunoblotted, and quantified (GAPDH was used as a loading control; see "Experimental procedures"). Fig. 1*C* shows immunoblots of wildtype FLAG-tagged *a*2 protein (WT *a*2–2FLAG), and the similarly epitope-tagged cutis laxa mutant subunit, $a2^{P405L}$ ($a2^{P405L}$-2FLAG) expressed transiently in HEK 293 cells, with and without Endo H treatment of the whole-cell lysates. WT *a*2–2FLAG was observed as a 110-kDa band, and upon Endo H treatment its relative mobility was reduced to 105 kDa, representing the deglycosylated *a*2–2FLAG. The mutant $a2^{P405L}$-2FLAG was also observed as a 110-kDa band, and upon Endo H treatment its relative mobility was reduced to 105 kDa, representing the deglycosylated $a2^{P405L}$-2FLAG.

In the same manner, protein stability of $a2^{P405L}$ was assessed by transient expression of the mutant protein or its wildtype counterpart. After allowing 24 h of expression, the cells were incubated with or without 10 μg/ml of CHX, and were harvested after the indicated times for whole-cell lysate preparation (see "Experimental procedures"). Glycans were removed from all proteins, wildtype and mutant, prior to immunoblotting, by treatment with PNGase F. Fig. 1*D* shows quantitative band analysis of the immunoblots used to assess stability of $a2^{P405L}$-2FLAG transiently expressed in HEK 293 cells. All band intensities were normalized to GAPDH as a loading control, and to zero time controls. These data showed that $a2^{P405L}$-2FLAG was degraded at a significantly faster rate than WT *a*2 ($p < 0.05$), the mutant protein having a half-life of 13.4 ± 1.0 h compared with 23.8 ± 4.3 h for WT *a*2–2FLAG (see supporting Tables S1 and S2 for data and statistics for all stability assays in the present work).

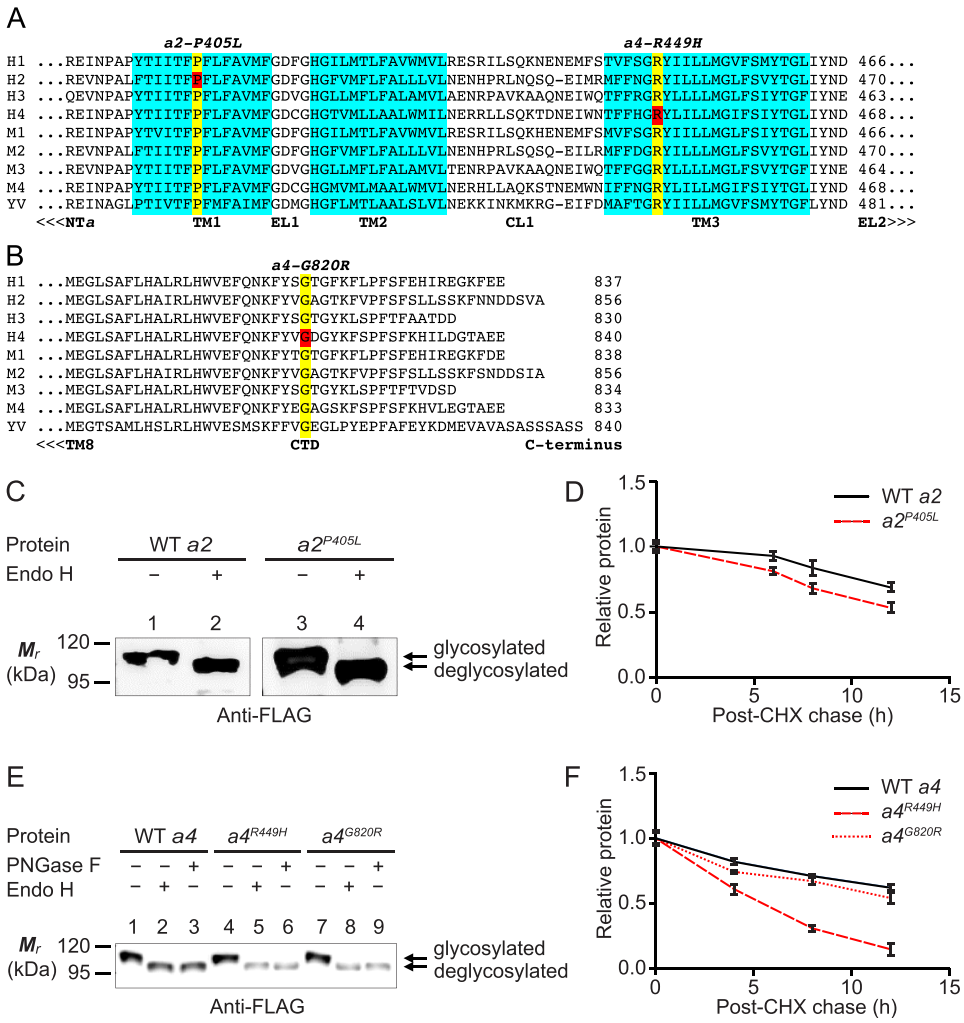

Figure 1. Glycosylation and stability of $a2^{P405L}$, $a4^{R449H}$, and $a4^{G820R}$. Sequence alignments show a high degree of conservation of residues affected by cutis laxa and dRTA mutations in V-ATPase *a* subunit proteins. The mutant proteins are all glycosylated, but stability is variably affected. *A*, amino acid sequence alignments from the end of the NT*a* domain to the end of TM3 of human *a*1–4 (*H1–4*), mouse *a*1–4 (*M1–4*), and yeast Vph1p (*YV*). Domains are indicated *below* alignments, in *bold*: *CL*, cytoplasmic loop; *EL*, extracellular (luminal) loop. *Cyan highlights* extrapolated from studies done in Vph1p indicate TM predictions (12). *Red* highlights indicate amino acids affected by human disease-causing mutations (noted above alignments). *Yellow* highlights indicate amino acids corresponding to the human mutations, within the subunit isoforms and species shown. *B*, alignments as in *A*, but of sequences from the end of TM8 to the C terminus, encompassing the cytoplasmic CTD. *C*, HEK293 cells were transfected with either WT *a*2–2FLAG (*WT a2*), or mutant $a2^{P405L}$-2FLAG (*$a2^{P405L}$*), and lysates treated with (+) or without (−) Endo H. *D*, same constructs as in *C*, but treated with 10 μM CHX for the time indicated; plots show band intensities quantified from immunoblots of post-CHX chase. Data were normalized to GAPDH and zero time control. *E*, same as *C*, except HEK 293 cells were transfected with WT *a4*–2FLAG (WT *a4*), mutant $a4^{R449H}$-2FLAG (*$a4^{R449H}$*), or mutant $a4^{G820R}$-2FLAG (*$a4^{G820R}$*), and lysates were treated with or without PNGase F or Endo H. *F*, same as *D*, except HEK 293 cells were expressing WT *a*4, mutant $a4^{R449H}$, or mutant $a4^{G820R}$. Data are representative of three independent biological experiments; *error bars* indicate ± S.D.

Glycosylation and stability of dRTA mutants, $a4^{R449H}$ and $a4^{G820R}$

Transient expression of FLAG-tagged human WT *a*4 and dRTA mutants was performed as for the *a*2 constructs. On immunoblotting, as shown in Fig. 1*E*, WT *a*4–2FLAG was observed as a 105-kDa band and, upon PNGase F and Endo H treatments, its relative mobility was reduced to 98 kDa, representing the deglycosylated *a*4–2FLAG. Similarly, $a4^{R449H}$-2FLAG and $a4^{G820R}$-2FLAG were observed as 105-kDa bands, and upon PNGase F or Endo H treatments their relative mobilities were reduced to 98 kDa, representing deglycosylated $a4^{R449H}$-2FLAG and $a4^{G820R}$-2FLAG. Thus, both $a4^{R449H}$ and $a4^{G820R}$ appeared to be *N*-glycosylated with Endo H-sensitive glycans, consistent with what was observed for WT *a*4.

To determine stability, WT *a*4 and the mutant proteins $a4^{R449H}$ and $a4^{G820R}$ were compared using CHX chase experiments, as described above; whole-cell lysates were prepared at the indicated time intervals and analyzed. Glycans were removed from all proteins, wildtype and mutants, by PNGase F treatment of cell lysates prior to immunoblotting; Fig. 1*F* shows quantitative band analysis of the immunoblots. All band intensities were normalized, as described above. Analysis of the data graphed in Fig. 1*F* showed that stability of $a4^{G820R}$-2FLAG, with a half-life of 13.7 ± 1.7 h, was reduced by only 20% ($p < 0.05$) relative to WT *a*4–2FLAG (17.0 ± 1.2 h); however, the half-life of $a4^{R449H}$-2FLAG (4.8 ± 0.39 h) was greatly reduced, by over 70% ($p < 0.01$) relative to WT *a*4–2FLAG.

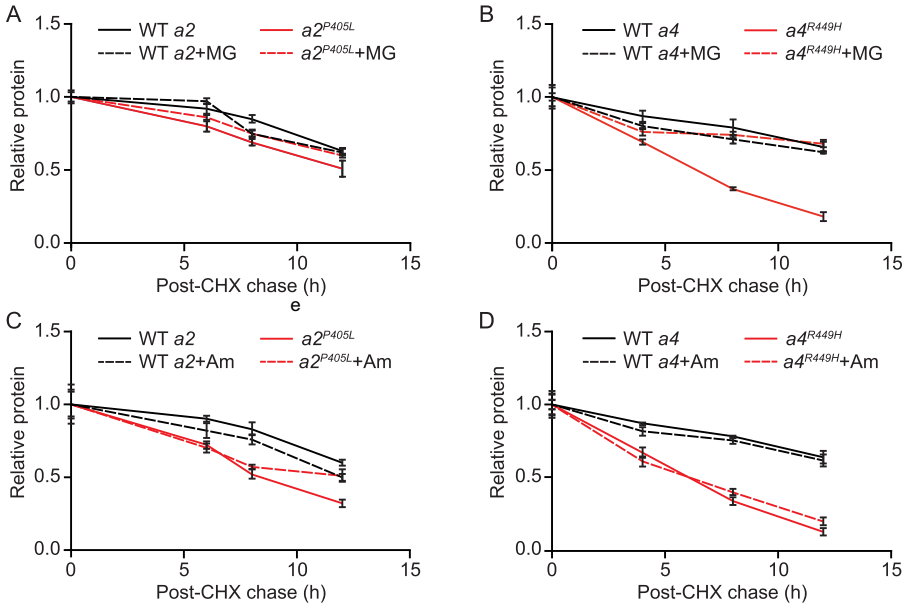

Figure 2. $a2^{P405L}$ is degraded in the proteasomal pathway with some lysosomal contribution, whereas $a4^{R449H}$ is degraded only in the proteasomal pathway. *A*, plot of quantified bands from anti-FLAG antibody-probed immunoblots of whole-cell lysates from WT *a*2–2FLAG and $a2^{P405L}$-2FLAG-transfected HEK 293 cells. Cells were treated with CHX (10 μg/ml) for the times indicated, with and without proteasome inhibitor (designated *MG*) as indicated. *B*, same as *panel A*, but cells were transfected with WT *a*4–2FLAG and $a4^{R449H}$-2FLAG constructs. *C*, same as *panel A*, but cells were treated with lysosomal inhibitor (designated *Am*) rather than proteasomal inhibitor. *D*, same as *panel B*, but cells were treated with lysosomal inhibitor. Data were normalized to GAPDH and zero time control and are representative of three independent biological experiments; *error bars* indicate ± S.D.

Pathways for degradation of unstable mutant proteins, $a2^{P405L}$ and $a4^{R449H}$

The stability of the $a4^{G820R}$ mutant subunit was not greatly different from wildtype, but the $a2^{P405L}$ and $a4^{R449H}$ mutants were clearly unstable. It was of interest to further characterize whether degradation of the latter two mutants was via the proteasomal pathway or the lysosomal pathway. After expression of $a2^{P405L}$-2FLAG and $a4^{R449H}$-2FLAG in HEK 293 cells, CHX chase experiments were done with and without either an inhibitor of proteasomes (10 μM MG132), or lysosomes (25 mM NH_4Cl), as previously described (25). Fig. 2 shows quantitative band analyses for the immunoblots loaded with WT *a*2–2FLAG and $a2^{P405L}$-2FLAG, or WT *a*4–2FLAG and $a4^{R449H}$-2FLAG, before and after MG132 treatment. Analysis of data in Fig. 2*A* showed that stability of the $a2^{P405L}$-2FLAG construct (half-life 13.4 ± 1.4 h) was 64% that of WT *a*2–2FLAG (half-life 21.0 ± 1.6 h); however, after proteasomal inhibition, the degradation rates of $a2^{P405L}$-2FLAG (half-life 17.7 ± 0.69 h) and WT *a*2–2FLAG (half-life 17.8 ± 1.2 h) were indistinguishable ($p = 0.89$). Data for Fig. 2*B* showed that without proteasomal inhibition, the half-life of the mutant $a4^{R449H}$-2FLAG (5.6 ± 0.12 h) was 26% that of WT *a*4–2FLAG (21.3 ± 3.7 h; $p < 0.05$). After proteasomal inhibition, there was a highly significant decrease ($p < 0.01$) in the degradation rate of $a4^{R449H}$-2FLAG (half-life 5.6 ± 0.12 h before treatment, 21.5 ± 1.5 h after), with restoration of stability to levels exceeding that of WT *a*4–2FLAG with the same treatment (half-life 17.2 ± 1.0 h). Data for Fig. 2*C* showed that lysosomal inhibition partially restored stability of $a2^{P405L}$-2FLAG (half-life 7.8 ± 0.51 h before and 11.4 ± 1.0 h after treatment, $p < 0.01$), by about half (56%) of the difference between untreated mutant levels and treated wildtype levels. Finally, data from Fig. 2*D* showed that lysosomal inhibition had no significant effect ($p = 0.10$) on the degradation rate of $a4^{R449H}$-2FLAG (half-life 5.1 ± 0.15 h before treatment, 5.6 ± 0.34 h after treatment). Taken together, this suggested that degradation of $a2^{P405L}$ occurs both in the proteasomal and lysosomal pathway, whereas the degradation of $a4^{R449H}$ predominantly occurs in the proteasome.

a2 Pro-405 is required for Golgi trafficking, and a4 Arg-449 for ER exit

The apparently significant degradation of both $a2^{P405L}$ and $a4^{R449H}$ suggests that the mutant subunits fail to assemble into the V-ATPase complex; therefore, we conducted immunofluorescence localization experiments to establish whether there is colocalization of these mutant proteins with ER and/or Golgi compartment markers. Fig. 3, *A* and *B*, show colocalization studies of WT *a*2–2FLAG and $a2^{P405L}$-2FLAG with calnexin (ER marker) and syntaxin 6 (Golgi marker). Fig. 3*A* shows representative fluorescence photomicrography images of HEK 293 cells transfected with empty vector (*left-most panel*), WT *a*2–2FLAG (*middle panel*), and $a2^{P405L}$-2FLAG (*right-most panel*), probed with anti-FLAG antibody (*green*) and antibodies to the ER marker, calnexin (*red*). These images showed that $a2^{P405L}$-2FLAG (*green*) colocalized with calnexin at a rate similar to that seen for WT *a*2–2FLAG ($p = 0.073$). A similar experiment is shown in Fig. 3*B*, but using the Golgi marker protein, syntaxin 6 (*red*). The $a2^{P405L}$-2FLAG mutant protein appeared to colocalize with the Golgi marker at a rate lower than was apparent for WT *a*2–2FLAG ($p < 0.05$).

Fig. 3*C* shows representative fluorescence photomicrography images of control, empty vector-transfected cells (*left-most panel*), WT *a*4–2FLAG (*second from left*), $a4^{R449H}$-2FLAG (*second from right*), and $a4^{G820R}$-2FLAG (*right-most panel*) probed with anti-FLAG (*green*) and anti-calnexin (*red*) antibodies. The data suggested that $a4^{R449H}$-2FLAG colocalized

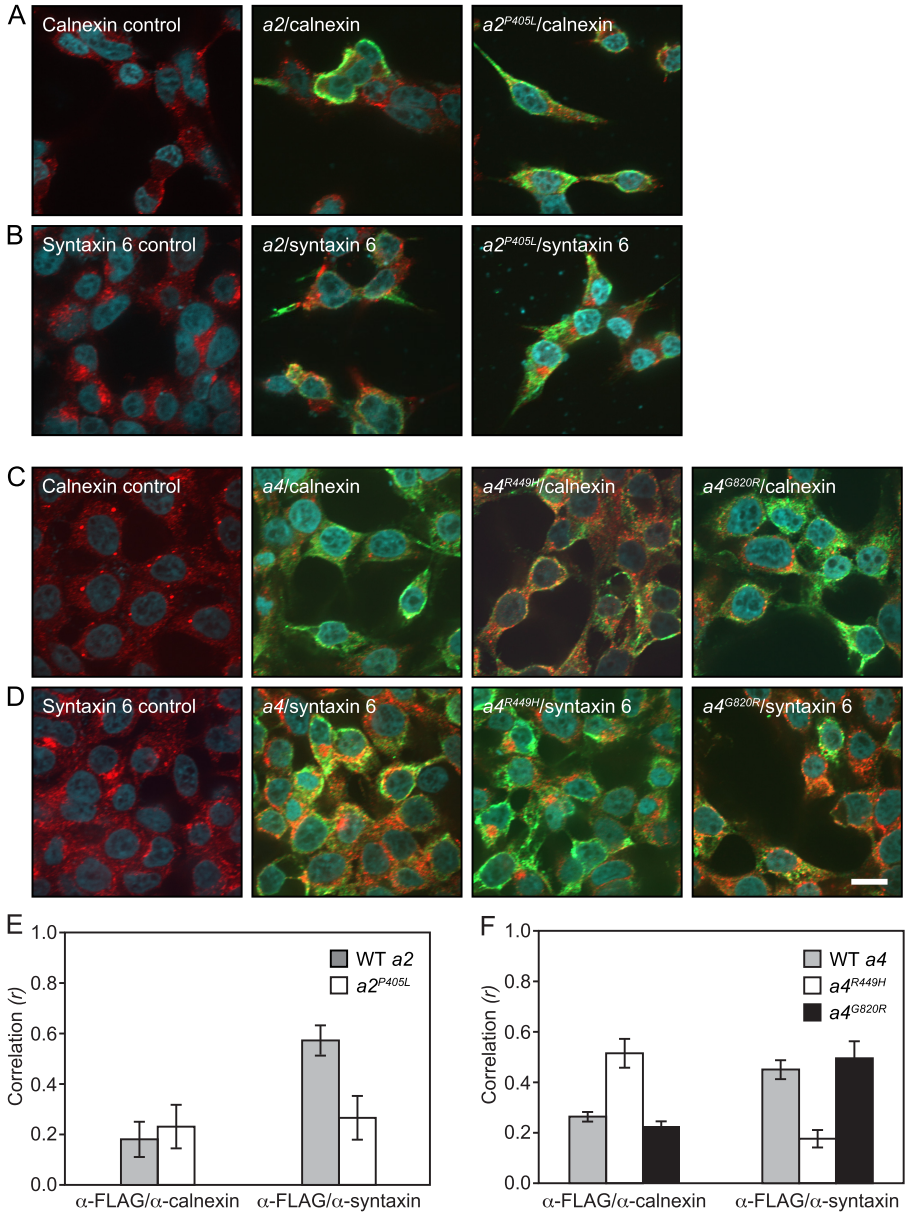

Figure 3. Localization of mutant *a* subunit proteins in the secretory pathway. *A*, representative confocal fluorescence images of empty vector-transfected HEK 293 cells (*left panel*), cells transiently transfected with WT *a2*-2FLAG (*middle panel*), or with $a2^{P405L}$-2FLAG (*right panel*). All panels show cells stained with anti-calnexin (*red*) and anti-FLAG (*green*). Nuclei are counterstained with DAPI (*blue*). *B*, same as *A*, except cells were stained with anti-syntaxin 6 (*red*) and anti-FLAG (*green*). *C*, fluorescence images of empty vector-transfected HEK 293 cells (*left-most panel*), cells transiently transfected with WT *a*4–2FLAG (*second from left*), with $a4^{R449H}$-2FLAG (*second from right*), or with $a4^{G820R}$-2FLAG (*right-most panel*). All panels show cells stained with anti-calnexin (*red*) and anti-FLAG (*green*). *D*, same as *C*, except cells were stained with anti-syntaxin 6 (*red*) and anti-FLAG (*green*). *E*, quantitative colocalization analysis of data in *panels A* and *B*. Ordinate is Pearson's correlation coefficient (*r*). Results show that $a2^{P405L}$ colocalized with calnexin at a rate similar to that of WT *a*2, but there was significantly less colocalization with syntaxin 6 compared with WT *a*2. *F*, quantitative colocalization analysis of data in *panels C* and *D*. Results show that $a4^{R449H}$ is mostly retained in the ER. Images are representative of 20 images (10–15 cells/image) each from three independent biological experiments.

with the ER marker, calnexin, at a higher rate than the WT *a*4–2FLAG ($p < 0.05$), whereas $a4^{G820R}$-2FLAG was similar to WT *a*4–2FLAG in this respect ($p = 0.081$). Fig. 3*D* shows representative micrographs of the same cell series as in Fig. 3*C*, but probed with anti-FLAG (*green*) and anti-syntaxin 6 (*red*) antibodies. The mutant protein, $a4^{R449H}$-2FLAG, colocalized with syntaxin 6 at a lower rate than the WT *a*4–2FLAG ($p < 0.05$), whereas $a4^{G820R}$-2FLAG was again similar to the WT *a*4–2FLAG in this respect ($p = 0.090$).

Fig. 3*E* shows colocalization analysis of images represented in Fig. 3, *A* and *B*, revealing that $a2^{P405L}$-2FLAG colocalized with calnexin in the ER, the same as WT *a*2–2FLAG. The localization of $a2^{P405L}$-2FLAG to Golgi (syntaxin 6), however, was reduced with reference to the wildtype ($p < 0.001$; $r = 0.5–0.8$). Similarly, Fig. 3*F* shows colocalization analysis of images represented in Fig. 3, *C* and *D*, revealing significant retention of $a4^{R449H}$-2FLAG in the ER, and significantly lower association with the Golgi marker, compared with WT *a4* ($p < 0.001$; $r = 0.5–0.8$). The $a4^{G820R}$ mutant, on the other hand, was indistinguishable from wildtype in these respects ($p = 0.081$ for calnexin, $p = 0.090$ for syntaxin 6).

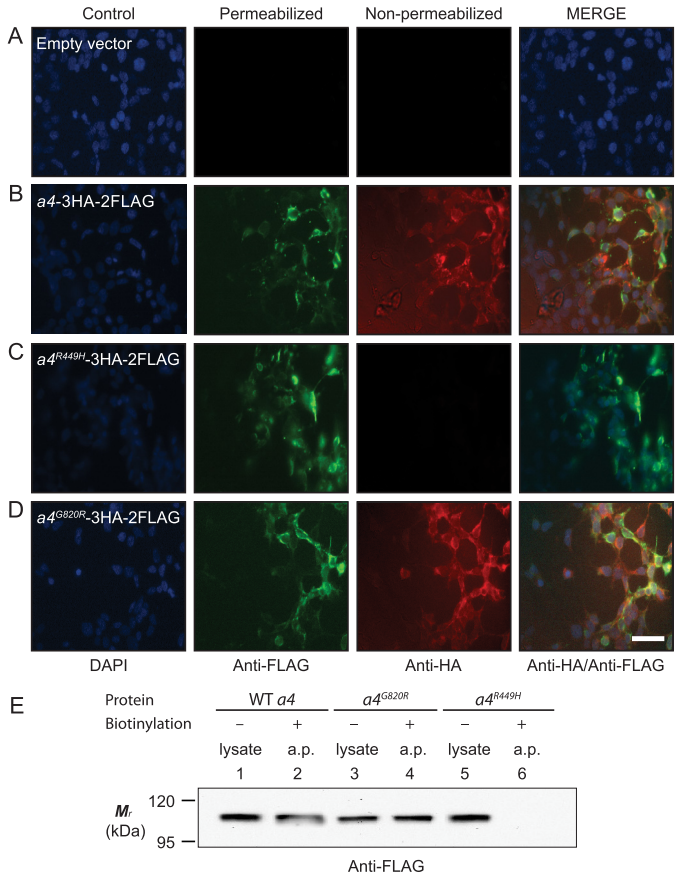

Figure 4. Defective cell-surface expression of $a4^{R449H}$. Fluorescence photomicrograph images show DAPI nuclear staining (*blue*) of HEK 293 cells transfected as indicated (*left-most panels*), fluorescent double antibody staining, first with anti-HA on non-permeabilized cells (*second from left panels*), followed by anti-FLAG after cell permeabilization (*second from right panels*), and merged images (*right-most panels*). Staining of non-permeabilized cells with anti-HA antibody indicated cell-surface accessibility of the epitope tag. *A*, empty vector-transfected (*control*) cells stained with anti-FLAG (*green*) and anti-HA (*red*). *B*, same as *A*, but cells were transfected with WT *a*4–3HA-2FLAG. *C*, same as *A*, but cells were transfected with WT $a4^{R449H}$-3HA-2FLAG. *D*, same as *A*, but cells were transfected with WT $a4^{G820R}$-3HA-2FLAG. The *scale bar* in the *bottom right panel* is 5 μm; all panels are of the same magnification. Each panel is representative of 20 micrographs obtained from 3 independent experiments. *E*, surface proteins of intact transfected cells subjected to biotinylation followed by streptavidin affinity purification (*a.p.*) and immunoblotting; blots were probed with anti-FLAG antibody (three independent experiments); *lane 1* (from left), whole-cell lysate from WT *a*4-transfected HEK 293 cells (*lysate*); *lane 2*, surface protein biotinylation showing surface protein fraction from cells transfected with WT *a*4 (*a.p.*); *lanes 3 and 4*, same as *lanes 1* and *2*, except cells were transfected with $a4^{G820R}$; *lanes 5* and *6*, same as *lanes 1* and *2*, except cells were transfected with $a4^{R449H}$. Blot is representative of three independent biological experiments.

Defective cell-surface expression of $a4^{R449H}$

As shown above, $a4^{R449H}$ was unstable relative to WT *a*4, was retained in the ER, and was ultimately degraded in the proteasome. To further its characterization, it was of interest to determine whether any of the mutant protein was able to traffic to its normal location at the cell surface. To assess cell-surface expression (Fig. 4), *a*4 was tagged with both HA in extracellular loop II (ELII) and FLAG at the end of the C terminus. We have shown ELII is the site of *N*-glycosylation within subunit *a*1–*a*4 (25, 26) indicating that ELII is luminal/extracellular. In contrast, we and others have shown that the C-terminal domain is cytoplasmic (12, 25, 26). Comparing the accessibility of either epitope in permeabilized *versus* non-permeabilized cells can determine whether *a*4 is expressed on the cell surface. In permeabilized cells, one would expect that both cytoplasmic and extracellular epitopes would be assessable to fluorescently-labeled antibodies; in non-permeabilized cells, only HA on the extracellular EL2, would be available. Fig. 4, *A–D,* shows representative fluorescence micrographs of HEK 293 cells transfected with WT *a*4–3HA-2FLAG, $a4^{R449H}$-3HA-2FLAG, or $a4^{G820R}$-3HA-2FLAG, double-stained with anti-HA (*red*) on non-permeabilized cells followed by cell permeabilization and staining with anti-FLAG (*green*). Total protein expression is represented by anti-FLAG (*green*) staining, and cell-surface expression by anti-HA (*red*) staining. Fig. 4*A* shows empty vector-transfected (*control*) cells stained, Fig. 4*B* shows intracellular as well as cell-surface expression for cells transfected with WT-*a*4–3HA-2FLAG, and Fig. 4*C* shows only intracellular expression in cells transfected with WT-$a4^{R449H}$-3HA-2FLAG, with no cell-surface expression detected. Fig. 4*D* shows intracellular, as well as cell-surface expression for cells transfected with WT-$a4^{G820R}$-3HA-2FLAG, a mutant that has a half-life similar to that of WT *a4*.

To confirm the above findings for *a*4 subunits, which are expected to traffic ultimately to the plasma membrane, cell-surface proteins of intact cells were biotinylated, and the biotinylated proteins were then affinity purified for further assessment (see "Experimental procedures"). Fig. 4*E* shows an immunoblot of the whole-cell lysates and the cell-surface fraction from cells that were transfected with WT *a*4–2FLAG, $a4^{R449H}$-2FLAG, or $a4^{G820R}$-2FLAG. WT *a*4–2FLAG and $a4^{G820R}$-2FLAG were expressed on the surface, as expected, but there was no cell-surface expression of $a4^{R449H}$-2FLAG. This result confirms the immunofluorescence findings in Fig. 4, *A–D*, suggesting that $a4^{R449H}$ is largely retained in the ER.

$a4^{R449H}$ shows increased association with VMA21

As demonstrated above, $a2^{P405L}$-2FLAG and $a4^{R449H}$-2FLAG had substantially shorter half-lives and defective Golgi and ER localization, as compared with their wildtype counterparts. It was of interest to characterize the effect of these mutations on their incorporation into the V-ATPase complex. The assembly of human V-ATPase is not well characterized, but studies in yeast have revealed that biosynthesis of V_0 in the ER is dependent on three assembly factors, Vma12p, Vma21p, and Vma22p (7). Due to the high homology between mammalian *a* subunit and the yeast ortholog, Vph1p, a similar biosynthetic mechanism was expected. VMA21, the human ortholog of yeast Vma21p, is the only characterized human V-ATPase assembly factor (29). VMA21 is required for incorporation of the *a* subunit into the V_0 subcomplex, but the dissociation of the *a* subunit from V_0 is required for further V_1–V_0 assembly. Thus, prolonged association of VMA21 with V_0 inhibits the formation of the V-ATPase holocomplex (30, 31). Fig. 5, *A–C,* show representative immunoblots loaded with immunoprecipitated fractions that were pulled down with anti-FLAG antibody from lysates of HEK 293 cells transfected with WT *a*2–2FLAG, $a2^{P405L}$-2FLAG, WT *a*4–2FLAG, $a4^{R449H}$-2FLAG, or $a4^{G820R}$-2FLAG and immunoblotted with either anti-VMA21 or anti-B1 antibodies. Protein band quantification

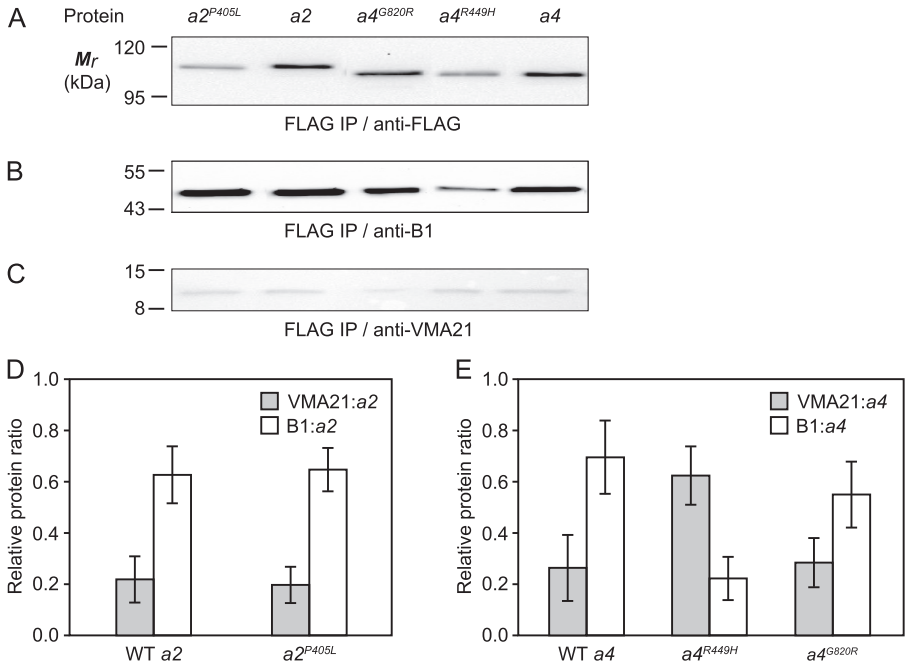

Figure 5. Association of *a* subunit with V-ATPase assembly chaperone, VMA21, and V_1 marker, ATP6V1B1. HEK 293 cells were transfected with WT and mutant FLAG-tagged constructs. After 24 h expression, whole-cell lysates were immunoprecipitated with anti-FLAG antibody. *A–C*, immunoprecipitates were blotted and probed with anti-FLAG (*A*), anti-B1 (*B*), or anti-VMA21 (*C*) antibodies. *D*, quantification of WT and mutant *a*2 associations with VMA21 and B1 in blots shown in *panels A–C*. No significant differences were observed between WT and mutant *a*2 associations with either VMA21 or B1. *E*, quantification of WT and mutant *a*4 associations with VMA21 and B1 in blots shown in *panels A–C*. Results showed significantly higher association of $a4^{R449H}$ with VMA21 ($p < 0.05$), and reduced association with B1 ($p < 0.05$), compared with WT *a*4. No significant difference was seen for $a4^{G820R}$ ($p = 0.064$ for association with VMA21, $p = 0.090$ for association with B1). Images are representative of 20 images (10–15 cells/image) each from three independent biological experiments; *error bars* are ±S.D.

analysis (Fig. 5, *D* and *E*) showed a difference between the mutant protein, $a4^{R449H}$-2FLAG, and its wildtype counterpart. The mutant had a significantly higher association ($p < 0.05$) with VMA21 (representing $a–V_0$ assembly), and a lower association with B1 (representing $V_1–V_0$ assembly) compared with wildtype *a*4 (Fig. 5*E*). Interestingly, there was no significant difference ($p = 0.12$) between the association of $a4^{G820R}$-2FLAG or $a2^{P405L}$-2FLAG with either B1 or VMA21, compared with their wildtype counterparts.

a4 Gly-820 resides within the putative proton pathway

As shown above, the $a4^{G820R}$-2FLAG, compared with WT, showed only a small or insignificant difference in terms of protein stability, localization in the secretory pathway, or cell-surface expression. Therefore, it remained of interest to determine the mechanism by which the $a4^{G820R}$ mutation causes dRTA. In an attempt to address this, we constructed a homology model for the CT*a* domain of the human *a4* subunit, based on a recent model for the CT*a* domain of yeast Vph1p. The latter was built based on low-resolution X-ray crystallography, high-resolution cryo-EM, mutagenesis studies, and analysis of evolutionary covariance (23). This model showed the locations of highly conserved, key functional residues within the proton translocation pathway, or proton channel. In a similar manner, we reconstructed the same residues within our human *a*4 model, and found that the *a*4 Gly-820 residue was located within the putative interface of the proton translocation pathway (Fig. 6, *A* and *B*). We created a second homology model for the $a4^{G820R}$ mutant protein (Fig. 6*C*) and showed that the positively-charged side chain of the mutant *a*4 Arg-820 residue possibly interferes with the proton pathway by forming a salt bridge (3.2 Å) with the adjacent negatively-charged residue, Glu-729. The latter amino acid has been previously recognized as an important residue for proton translocation (32).

Discussion

a2 Pro-405, a4 Arg-449, and a4 Gly-820 are conserved and crucial for function

Mutation of the V-ATPase *a*2 subunit amino acid residue Pro-405 results in cutis laxa, and *a*4 mutations in residues Arg-449 and Gly-820 result in dRTA. In an effort to understand how these missense point mutations can lead to disease, we first conducted multiple amino acid alignments, which revealed that the residues of interest were highly conserved (Fig. 1, *A* and *B*). The *a*2 Pro-405, *a*4 Arg-449, and *a*4 Gly-820 residues reside within TM1, TM3, and the CTD, respectively, which are highly conserved domains in species ranging from human to yeast. By characterizing the effects that these mutations have on *a* subunit glycosylation, structural stability, trafficking, and assembly, we hoped to elucidate their disease mechanisms and also add to the as yet limited understanding of structural/functional domains within human V-ATPases, ultimately to provide a basis for rational drug design.

Human $a2^{P405L}$ and $a4^{R449H}$ are N-glycosylated, but are unstable and $a4^{R449H}$ degraded predominantly in the proteasomal pathway

We have previously shown that human *a*1–*a*4 subunits are *N*-glycosylated and that this is important for subunit stability (25, 26). In the present study, results of Fig. 1, *C* and *E*, show that

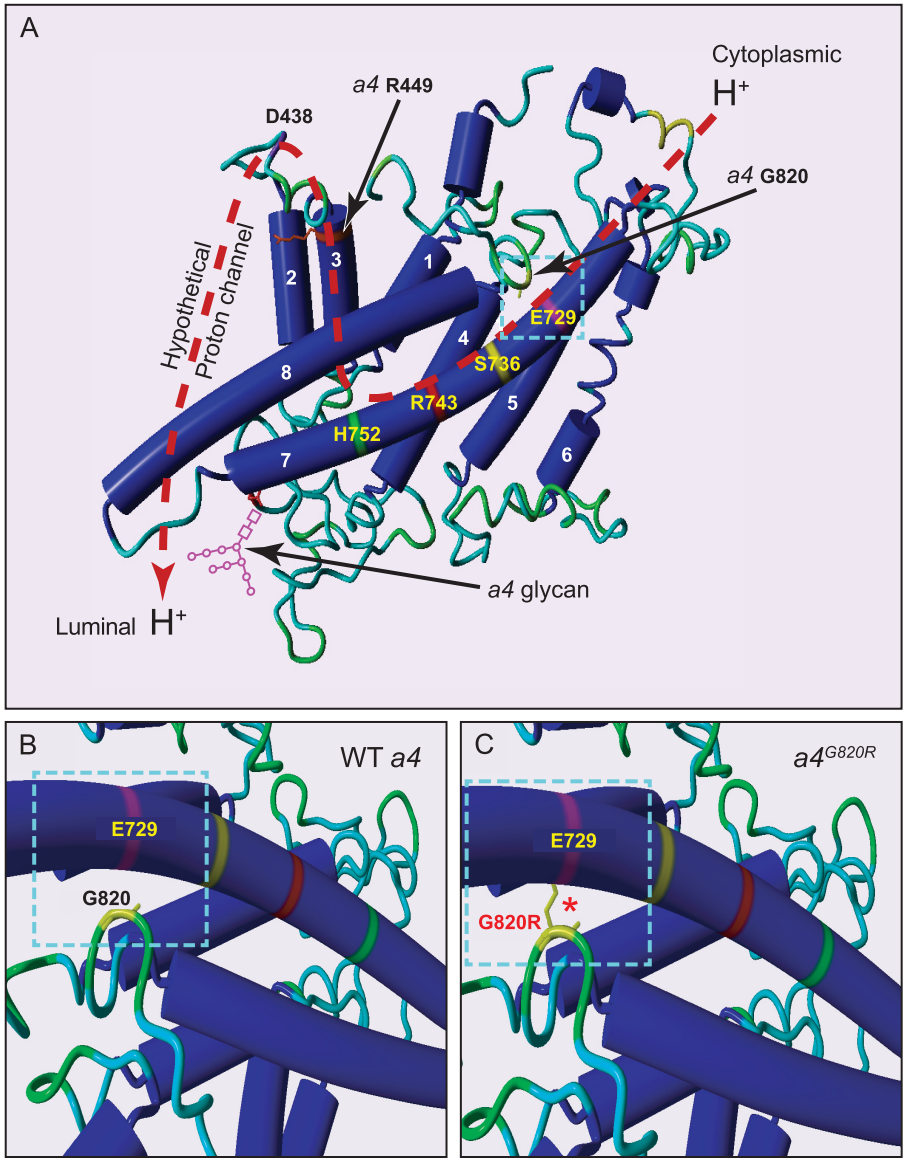

Figure 6. *a4* Gly-820 resides within the putative proton translocation pathway. *A*, homology model for C-terminal integral membrane (CT*a*) domain of the human *a*4 subunit. This model was constructed based on the recent high-resolution cryo-EM structure and evolutionary covariance analysis for the yeast *a* subunit, Vph1p (23). The indicated residues are highly conserved and essential for proton translocation. The *red dashed line* shows the hypothetical proton channel from the cytoplasmic side of the membrane to the luminal space. *Cyan dashed box* indicates the subregion where amino acid residue Gly-820 is located. *B*, shows the close proximity of Gly-820 and the highly conserved Glu-729, a residue thought to be key in proton translocation (10, 32, 38). *C*, illustrates how the G820R mutation may result in a salt-bridge interaction (*red asterisk*) between Glu-729 and Arg-820, possibly distorting or blocking the proton channel, resulting in inhibition of proton translocation, and providing a causative explanation for the role of the $a4^{G820R}$ mutation in dRTA.

mutant proteins, $a2^{P405L}$, $a4^{R449H}$, and $a4^{G820R}$, were all *N*-glycosylated, and all with Endo H-sensitive high-mannose or hybrid glycan moieties. Moreover, $a2^{P405L}$ and $a4^{R449H}$, but not $a4^{G820R}$, showed a much higher rate of turnover (*i.e.* decreased stability) relative to their respective wildtype subunit (Fig. 2). These results also showed that turnover rates of $a2^{P405L}$ and $a4^{R449H}$ could be restored to wildtype levels by treatment with the proteasomal inhibitor, MG132. Treatment with the lysosomal inhibitor, NH_4Cl, had no significant effect on the turnover rate of $a4^{R449H}$ and modestly reduced the turnover rate of $a2^{P405L}$. This suggested that $a4^{R449H}$ was degraded predominantly in the proteasomal pathway, which is activated in response to the presence of misfolded proteins in the ER (33), with some degradation of the former occurring also in the lysosomal pathway.

Within this study, we tagged both WT and mutant subunits with C-terminal epitopes. We, and others, have shown that a variety of different epitope types and sizes inserted at the extreme C-terminal domain of the mammalian V-ATPase *a* subunit does not appear to affect activity or stability (25, 26, 34–36). In yeast, we were able to show that introducing green fluorescent protein, a 238-amino acid, 26.9-kDa polypeptide, to the C-terminal of Vph1p, the yeast V-ATPase *a* subunit, did not affect subunit stability, assembly, function, and trafficking with respect to endogenous Vph1p (12).

a2 Pro-405 is required for Golgi trafficking, and a4 Arg-449 for ER exit

The relatively high degradation rates of both $a2^{P405L}$ and $a4^{R449H}$ in the proteasomal pathway suggested that these sub-

units fail to assemble into the V-ATPase complex and therefore fail to traffic to their normal destinations. Despite the higher turnover rate of $a2^{P405L}$ relative to the wildtype (Fig. 2, *A* and *C*), however, quantification of colocalization of $a2^{P405L}$ with calnexin showed no significant difference in association of $a2^{P405L}$ with calnexin, compared with WT *a*2 ($p = 0.073$). Additionally, however, $a2^{P405L}$ showed significantly less association ($p < 0.05$) with the Golgi marker, syntaxin 6 (Fig. 3*E*), which suggested that the $a2^{P405L}$ mutation results in misprocessing that leads to defective Golgi trafficking, but not ER retention. In contrast, quantification of colocalization analysis for $a4^{R449H}$ and $a4^{G820R}$ with the ER-resident marker, calnexin (Fig. 3, *C* and *F*), revealed a significantly higher colocalization of $a4^{R449H}$ with calnexin ($p < 0.05$), suggesting ER retention of $a4^{R449H}$, but not of $a4^{G820R}$, which was not different from wildtype *a4* in that respect ($p = 0.081$). However, the exact mechanism of $a4^{R449H}$ ER retention remained to be investigated. Taken together, these observations suggest that the *a*2 Pro-405 and *a*4 Arg-449 residues within TM1 and TM3, respectively, are essential for human *a*2 and *a*4 stability, and for their trafficking in the secretory pathway.

a4 Arg-449 is crucial for cell-surface expression and a-V_o association

We have previously shown experimentally that the exogenously expressed WT *a*4 is able to traffic to the plasma membrane of HEK 293 cells (25). In the current study we have used the same strategy to determine the effect of the mutations in $a4^{R449H}$ and $a4^{G820R}$ on cell-surface expression. Fig. 4, *B* and *D*, showed that both WT *a*4 and $a4^{G820R}$ were able to traffic to the cell surface, whereas $a4^{R449H}$ showed defective cell-surface expression (Fig. 4*C*). The same findings were subsequently confirmed by cell-surface biotinylation (Fig. 4*E*).

It was of interest also to determine the effect of the mutations under investigation on formation of the V-ATPase holocomplex. To that end, we specifically characterized the association of $a2^{P405L}$, $a4^{R449H}$, and $a4^{G820R}$ with the only characterized human V-ATPase assembly factor, VMA21. Protein band quantification of co-immunoprecipitates (Fig. 5*E*) revealed that $a4^{R449H}$ had a significantly higher association ($p < 0.05$) with VMA21. In yeast, the assembly chaperone Vma21p assembles with V_0-associated *a* subunits, and dissociates only after V_0 exits the ER (37); dissociation of Vma21p from V_0 is required for V_1–V_0 assembly, and prolonged Vma21p-V_0 association reduces V_1–V_0 assembly. We propose that the significantly higher association observed between $a4^{R449H}$ and VMA21 indicates a prolonged association of $a4^{R449H}$-V_0 with VMA21 that leads to failure of V_1–V_0 assembly, ER retention of $a4^{R449H}$, and ultimately its proteasomal degradation, resulting in defective cell-surface expression.

a4 Gly-820 is a functional residue residing in the putative proton pathway

The *a*4 Gly-820 residue is highly conserved among species (Fig. 1*B*). Due to the lack of a mammalian model, the mechanism of the $a4^{G820R}$ dRTA–causing mutation has been studied previously only in yeast. One of these studies reported that the $a4^{G820R}$ mutation in the yeast homolog, Vph1p, did not affect pump assembly or targeting but decreased V-ATPase hydrolytic and proton pumping activities by 83–85% (10). Another study in the yeast *a* subunit showed that the $a4^{G820R}$ homologous mutation ($Vph1p^{G812R}$) was associated with severe loss of proton translocation (by 78%) and a moderate decrease in ATPase activity (by 36%). This study also showed that the *a4* Gly-820 residue lies within the domain that interacts with the glycolytic enzyme, phosphofructokinase-1 and that the $a4^{G820R}$ equivalent mutation inhibited this interaction (38). In the present work we used exogenous expression in HEK 293 cells to investigate the role of this mutation in protein stability, glycosylation, and trafficking in the secretory pathway and the plasma membrane, and our results showed that the stability of $a4^{G820R}$ was only mildly affected (Fig. 1*F*) and trafficking to the Golgi and plasma membrane were not discernably altered (Figs. 3*D* and 4*D*).

In an attempt to obtain further insights into how *a*4 G820R might impact V-ATPase function, we used the recently published atomic model synthesized from studies of *Thermus thermophilus* and *Saccharomyces cerevisi*ae V-ATPase and bovine F-ATPase (23) as a template to construct a 3D human *a*4 C-terminal domain model (Fig. 6*A*). The model revealed that the *a*4 Gly-820 residue interfaces with the proposed proton transport pathway. Furthermore, swapping arginine for glycine (*a*4 G820R) resulted in a putative salt bridge (3.2 Å) with the adjacent negatively charged residue *a*4 Glu-729 (compare Fig. 6, *B* with *C*), which is also highly conserved and is thought to be important for proton translocation (32). Therefore, we proposed that the $a4^{G820R}$ mutation likely causes dRTA by forming a salt bridge that sterically interferes with the structure of the proton channel and consequently with proton translocation. It might do this directly, by blocking the proton channel physically (*i.e.* in its immediate vicinity), or allosterically by altering the conformation of the CTD more extensively. Some conformational change must be occurring to be consistent with the previous observation that the mutation also inhibits the interaction of the *a* subunit with phosphofructokinase-1 (38), the binding of which must occur at a cytoplasmically accessible site; however, this does not preclude the possibility that the putative salt bridge resulting from the G820R mutation both blocks the proton pathway directly and causes extended conformational changes in the CTD.

Conclusion

Characterization of highly conserved residues implicated in diseases has been successfully used by others as a strategy for determining protein domain function and to inform targeted drug discovery (39–41). For example, deletion of the highly conserved residue Phe-508 (ΔF508) in the human cystic fibrosis transmembrane-conductance regulator (CFTR) leads to cystic fibrosis. The ΔF508 mutation results in protein misfolding, misprocessing, and aberrant trafficking (42). Characterization of the molecular mechanism of ΔF508 CFTR disease causation has led to the development of molecular chaperone approaches to correct CFTR folding and promote its trafficking to its normal functional destination, yielding a promising approach for treatment of ΔF508 cystic fibrosis (41).

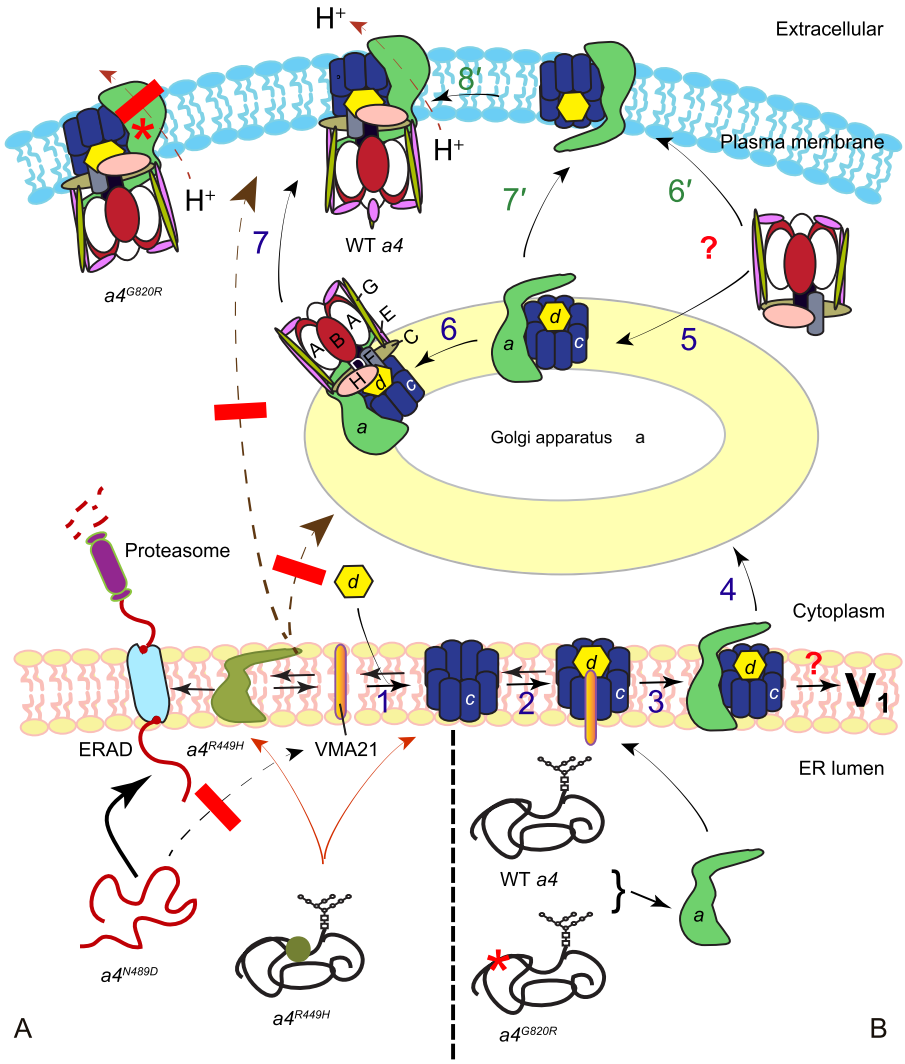

Figure 7. Model for human *a4* trafficking in the secretory pathway and to the plasma membrane. Steps *1*–*7* and *6′*–*8′* suggest two putative mechanisms of mammalian V-ATPase assembly. First, within the ER, the VMA21 assembly factor facilitates the assembly of subunit *a* into the V_0 subcomplex (steps *1*–*3*). The assembled V_0 subcomplex is subsequently trafficked to Golgi (step *4*), assembled with the V_1 subcomplex within the Golgi (steps *5* and *6*), with the fully assembled V-ATPase complex targeted to the plasma membrane (step *7*). Alternatively, the V_0 subcomplex itself could traffic to the plasma membrane (*7′*) and only assemble with the V_1 subcomplex at the plasma membrane (steps *6′*–*8′*). *A*, an unglycosylated mutant, $a4^{N489D}$, which was described in a previous study (25), is unable to assemble into a V_0 subcomplex. It is retained in the ER and is targeted to the ERAD pathway for proteolysis. In contrast, the glycosylated $a4^{R449H}$ mutant described here assembles within the V_0 complex; however, it is ultimately degraded in the proteasome, and thus also fails to reach the plasma membrane. *B*, the glycosylated $a4^{G820R}$ assembles within the V_1V_0 complex and is trafficked to the plasma membrane but, unlike the wildtype complex, functional proton translocation appears to be inhibited by the mutation. *Red asterisks* symbolize the $a4^{G820R}$ mutation; a *dark green circle* symbolizes the $a4^{R449H}$ mutation; *red bars* indicate blockade of a pathway; V_1 subunits are indicated by *uppercase letters*; V_0 subunits are indicated by *lowercase italic letters*.

V-ATPase *a* isoforms are potential targets for therapeutics directed toward a number of diseases (1). Thus, a further understanding of the structural domains affecting *a* subunit folding, trafficking, membrane targeting, function, and regulation will enhance our ability to target specialized V-ATPases. We previously showed that *N*-glycosylation is required for *a* subunit stability, assembly, and trafficking to the plasma membrane (25, 26). In the present work we showed that $a2^{P405L}$ and $a4^{R449H}$ resulted in cutis laxa and dRTA through interfering with protein stability, and subsequent ER retention and degradation. $a4^{R449H}$ was degraded predominantly in the proteasomal pathway, whereas $a2^{P405L}$ was degraded in both proteasomal and lysosomal pathways. In summary, we have proposed a model for how we believe that the *N*-glycosylated *a*4 subunit is assembled, trafficked in the secretory pathway, and delivered to the plasma membrane (see Fig. 7). Our data also suggest routes to drug discovery such as screening for chemical chaperons to rescue *a* subunit folding to allow ER exit for treatment of cutis laxa and dRTA.

Experimental procedures

Enzymes and reagents

Restriction enzymes, Endo H (catalog number P0702S), and PNGase F (number P0704S) were from New England Biolabs (Whitby, Canada). Octaethylene glycol mono-*n*-dodecyl ether ($C_{12}E_8$) was from NIKKO Chemicals (Barnet Products, Englewood Cliffs, NJ). Bradford protein assay reagent (500-0006) was from Bio-Rad (Mississauga, Canada), 4′,6-diamidine-2′-phenylindole dihydrochloride (DAPI; 10236276001) was from

Roche Diagnostics (Mississauga, Canada), and CHX (CYC003) was from BioShop (Burlington, Canada). Phenylmethylsulfonyl fluoride (PMSF; P7626), protease inhibitor mixture (P8340), and the proteasome inhibitor *N*-(benzyloxycarbonyl)leucinyl-leucinylleucinal (MG132; C2211) were from Sigma. Dulbecco's modified Eagle's medium (DMEM; 11965092), Dulbecco's phosphate-buffered saline (DPBS; 1404182), heat-inactivated fetal bovine serum (16140071), penicillin/streptomycin mixture (15140122), phosphate-buffered saline (PBS; 10010023), 1× trypsin/EDTA (25200056), and the Novex ECL horseradish peroxidase (HRP) chemiluminescent substrate reagent kit (WP20005) were obtained from Gibco (Fisher Scientific, Whitby, Canada). GenJet *In Vitro* DNA Transfection Reagent (SL100488) was purchased from SignaGen Laboratories (Rockville, MD).

Antibodies

Mouse monoclonal IgG2b anti-calnexin (3H4A7; sc-130059), HRP-conjugated goat polyclonal IgG anti-rabbit IgG (sc-2004), mouse monoclonal IgG1 anti-glyceraldehyde-3-phosphate dehydrogenase (anti-GAPDH, 0411; sc-47724), and HRP-conjugated goat polyclonal IgG anti-mouse IgG (sc-2005) were purchased from Santa Cruz (Dallas, TX). Rabbit IgG anti-VMA21 antibody (HPA010972) was from Sigma. Rabbit polyclonal IgG anti-FLAG (ab1162) and mouse monoclonal IgG1 anti-syntaxin 6 (ab56656) were from Abcam (Cedarlane, Burlington, Canada). Alexa Fluor 568-conjugated goat polyclonal IgG anti-rabbit IgG (A-11011), Alexa Fluor 488-conjugated goat polyclonal IgG anti-rabbit IgG (A-11034), Alexa Fluor 568-conjugated goat polyclonal anti-mouse IgG (A-11004), and Alexa Fluor 488-conjugated goat polyclonal IgG anti-mouse IgG (A11001) were from Molecular Probes, Fisher Scientific.

cDNA constructs, plasmids, and cells

The pCMV6-XL4 plasmid carrying human *a*2-coding cDNA was purchased from Origene (SC115366). To prepare wildtype *a*2–2FLAG (with tandem C-terminal FLAG epitope tags), the insert was transferred from pCMV6-XL4 to pBlueScript SK^+, then tagged with 2FLAG (2 × DYKDDDDK) at its carboxyl terminus between XbaI/HindIII restriction sites. The 2FLAG-tagged construct was then transferred back to pCMV6-XL4 between APaI/HindIII sites. To prepare the $a2^{P405L}$-2FLAG mutant construct, the pCMV6-XL4 carrying WT *a*2–2FLAG was modified by inserting a synthetic fragment bearing the P405L mutation between BmgBI/pf1F1 sites (human *a*2 cDNA bp 1916–2487); the mutant synthetic cDNA was obtained from GeneArt in the PMA-T vector. WT *a*4–3HA-2FLAG was prepared as described previously (25). To prepare $a4^{R449H}$-3HA-2FLAG and $a4^{G820R}$-3HA-2FLAG, GeneArt synthetic cDNA bearing the R449H mutation was inserted between EcoRI/SapI sites, and the $a4^{G820R}$ fragment was inserted into the ApaI site in pcDNA3.1(+). Accession numbers for source sequences used in constructs are: human *a*2 (*ATP6V0A2*), NM_012463; human *a*4 (*ATP6V0A4*), NP_570856. The DNA sequences of all constructs were confirmed by commercial sequencing (ACGT Corp., Toronto, Canada). Human embryonic kidney cells (HEK 293; CRL-1573TM) were from the American Type Culture Collection (ATCC, Manassas, VA).

Cell culture and transfection

Liquid nitrogen-stored HEK 293 cells were rapidly thawed in a water bath at 37 °C followed by incubation in 75-cm^2 tissue culture flasks containing 17 ml of DMEM, supplemented with a 10% fetal bovine serum and 1% penicillin/streptomycin mixture, in a humidified 5% CO_2 incubator for 4 days at 37 °C. The cells, at 70–80% confluence, were trypsinized with 1 ml of 1× trypsin/EDTA and seeded into 6-well plates at a density of $4–7 \times 10^5$ cells/well and incubated for 24 h. Cells were subsequently transiently transfected with 1 μg/well of plasmid construct in a transfection complex containing GenJet reagent and plasmid DNA in a 3:1 ratio. The transfection complex was diluted to 200 μl of final volume with serum-free DMEM and incubated for 10 min prior to transfection. Post-transfection cells were incubated for 24 h and then harvested for protein expression analysis. There was no significant difference ($p < 0.05$) in cell viability between HEK 293 cells transfected with WT, mutant, or empty vectors (data not shown).

Protein expression analysis and assessment of glycosylation

Whole-cell lysates were prepared as previously described (25). Briefly, cells were harvested in 0.2 ml/well of lysis buffer (PBS containing 1% $C_{12}E_8$, 1 mM PMSF, and 1:100 (v/v) Protease Inhibitor Mixture) and incubated on ice for 30 min. Lysates were then centrifuged at 15,000 × *g* for 30 min at 4 °C, and supernatants were collected for further analysis. Protein concentrations of the supernatants were quantified using the Bradford protein assay.

Protein glycosylation was assessed by treatment of samples with either PNGase F or Endo H. Briefly, 30 μg of whole-cell lysate was denatured in 3 μl of 10× glycoprotein denaturation buffer (5% sodium dodecyl sulfate, 0.4 M dithiothreitol; New England Biolabs), the reaction mixture was adjusted to 20 μl and incubated at 65 °C for 10 min, then 2 μl of 10× Glyco Buffer was added (for PNGase F, 0.5 M sodium phosphate, pH 7.4, at 25 °C; for Endo H, 0.5 M sodium citrate, pH 7.5, at 25 °C). Subsequently, 2 μl of 10% (w/v) Nonidet P-40 (New England Biolabs) and 2,000 units of PNGase F, or Endo H, were added. The final volume was adjusted to 40 μl with distilled H_2O, incubated for 1 h at 37 °C, and then analyzed by immunoblotting.

Immunoblotting

Immunoblotting was conducted as previously described (25). Briefly, 30 μg of whole-cell lysate was loaded per well and subjected to 7% SDS-PAGE. Proteins were then transferred to nitrocellulose membrane and incubated overnight at 4 °C with 1:2,000–1:3,000 diluted primary antibodies (anti-FLAG, anti-B1, or anti-VMA21). 1:5,000 diluted anti-GAPDH was used in some experiments to provide loading controls. The blots were then incubated for 1 h at room temperature with 1:5,000 HRP-labeled secondary antibody and bands were developed with chemiluminescent substrate reagent.

Protein stability and protein band quantification

Protein stability was evaluated using the CHX chase assay. Briefly, HEK 293 cells were transfected with WT and mutant cDNA constructs and 24 h post-transfection the cells were

treated with 10 μg/ml of CHX with or without proteasomal inhibitor (10 μM MG132), or lysosomal inhibitor (25 mM NH_4Cl), for up to 12 h. The cells were subsequently harvested and whole-cell lysates were prepared for immunoblotting with anti-FLAG, and anti-GAPDH as a loading control.

Protein band quantification of CHX immunoblots was performed using Bio-Rad Quantity One 4.6.9 software. Briefly, band intensities were quantified after subtracting the background signals from band signals using the rolling-disc method. Relative protein levels were estimated after normalizing band intensities relative to GAPDH loading controls and zero time controls. Glycoproteins tend to run in SDS-PAGE as diffuse bands so, for more accurate comparison of unglycosylated bands with the more similar deglycosylated protein bands, whole-cell lysates were treated with PNGase F prior to immunoblotting to remove glycan moieties, yielding uniformly sharp protein bands.

Statistical analysis of the CHX chase data were done using GraphPad Prism 5 software. Non-linear curve fitting was done assuming a simple exponential one-phase decay model. Prior subtraction of background was accommodated by modifying the default model equation in GraphPad Prism as follows: exponential/one-phase decay model, $Y = (Y0) \times \exp(-K \times X)$. Automated curve fitting and non-linear regression analysis provided half-life times (h). For time 0, mean ± S.D. were obtained from data normalized to GAPDH only, then applied proportionately to the zero points normalized for GAPDH and zero time (*i.e.* 1.0). Data in figures were plotted point-to-point rather than as fitted exponential curves to preserve clarity of the original data. Mean ± S.D. values were derived from three independent experiments, and p values, representing significance of differences for comparisons, were derived from unpaired, two-tailed Student's t tests. Data analyses, including raw data, correlation coefficients (R^2) of fit of the one-phase exponential decay model, and half-life values and their standard deviations, are tabulated in supporting Table S1. The derived p values for comparisons are tabulated in supporting Table S2.

Co-immunoprecipitation

HEK 293 cells were transfected with WT and mutants cDNA constructs and whole-cell extracts were prepared in IP buffer (150 mM NaCl, 25 mM Tris HCl, pH 7.2, at 25 °C, containing 1% $C_{12}E_8$, 1:100 (v/v) Protease Inhibitor Mixture and 1 mM PMSF), as previously described (25). Co-immunoprecipitation of WT and mutants was conducted by treating 50 μg of whole-cell lysate with 5 μg of anti-FLAG antibody and incubating overnight at 4 °C with agitation. Antigen–anti-FLAG antibody immunocomplexes were pulled down by incubation with 100 μl (50% packed volume) of protein A-agarose beads for 2 h at room temperature with agitation. The antigen-coated beads were then incubated 5 min with SDS-PAGE sample buffer at 95 °C to elute the antigens. Antigen-containing supernatants were collected after centrifugation at 2,500 × g for 3 min and then immunoblotted with anti-FLAG, anti-B1, and anti-VMA21 antibodies.

Immunofluorescence and colocalization analysis

HEK 293 cells were grown on glass coverslips and transiently transfected with WT and mutant cDNA constructs. The cells were washed with DPBS and fixed with 3.7% (w/v) paraformaldehyde for 15 min at room temperature. Subsequently, cells were permeabilized with DPBS containing 0.2% Triton X-100 at room temperature for 15 min. Cells were then blocked with DPBS containing 5% bovine serum albumin for 1 h at room temperature, followed by immunostaining with anti-FLAG (1:1,000), anti-calnexin (1:500), or anti-syntaxin 6 (1:500) antibodies in DPBS containing 5% bovine serum albumin for 45 min at room temperature. Cells then were washed 3 times with DPBS and immunostained with fluorescent second antibodies (1:500) for 45 min at room temperature. Nuclei were stained with 0.1 mg/ml of DAPI in DPBS for 10 min and cells were mounted with ProLong Gold Antifade Reagent (Fisher Scientific). Photomicrography images were acquired using a Quorum Spinning Disk Confocal System equipped with a Hamamatsu C9100-13 EM-CCD, Yokogawa CSU X1 scan head, and Improvision Piezo focus drive (Imaging Facility, Hospital for Sick Children, Toronto, Canada).

Colocalization quantification of 20 images (10–15 cells/image) each from three independent experiments was conducted using Volocity version 6.3 3D image analysis software (PerkinElmer Life Sciences, Woodbridge, Canada). Colocalizations of two fluorescent signals (*red* and *green*) were quantified and expressed as Pearson's correlation coefficients (r). Significance of differences between WT and mutants were estimated using two-tailed Student's t tests.

Cell-surface biotinylation

Cell-surface labeling was performed using EZ-Link NHS SS-Biotin reagent (Pierce 21328; Fisher Scientific), as described previously (25). Briefly, HEK 293 cells were transiently transfected and, 24 h post-transfection, the cells were incubated with 1 mg/ml of freshly prepared EZ-Link NHS-SS-Biotin for 1 h at 4 °C with gentle agitation. The cells were then incubated with ice-cold quenching buffer (192 mM glycine, 25 mM Tris, pH 8.3, at 25 °C) to remove excess biotin. Cells were harvested in 0.4 ml of ice-cold RIPA buffer (150 mM NaCl, 1% sodium deoxycholate, 0.1% SDS, 1% Triton X-100, 1 mM EDTA, and 10 mM Tris-HCl, pH 7.5, at 25 °C) containing Protease Inhibitor Mixture (1:100 v/v) and 1 mM PMSF, and were incubated for 30 min on ice, then centrifuged at 15,000 × g for 30 min at 4 °C. Supernatants were collected, and biotinylated cell-surface proteins were affinity purified by incubating supernatants with 100 μl (50% packed volume) of streptavidin-agarose beads (Pierce 20347; Fisher Scientific) for 2 h at 4 °C. The eluted, biotinylated cell-surface proteins and total lysate proteins were analyzed by 7% SDS-PAGE and immunoblotted, as previously described (25).

Structural modeling of human a4 subunit

Homology modeling of the integral membrane domain of the human *a*4 subunit was generated by SWISS-MODEL, using the yeast *a* subunit ortholog, Vph1p, as a template (PDB code 5I1M) (23, 43). Subsequently, the model was corrected and the 3D representation was generated using the 3D graphical

YASARA interface (44). A 3D representation of $a4^{G820R}$ was generated after substituting Gly-820 with Arg, using the YASARA FoldX plug-in.

Author contributions—S. E., N. K., R. A. F. R., and M. F. M. conceptualized, planned, and analyzed experimental work. S. E. performed all experiments except those represented in Fig. 1*C*, which were performed by J. W. K.; S. E. and Y. Y. designed and prepared constructs used in the study; and Y. Y. provided additional technical expertise. S. E. and N. K. wrote the manuscript and prepared figures.

References

1. Kartner, N., and Manolson, M. F. (2016) The vacuolar proton ATPase (V-ATPase): regulation and therapeutic targeting. in *Regulation of Ca^{2+}-ATPases, V-ATPases and F-ATPases* (Chakraborti, S., and Dhalla, N. S., eds) pp. 407–437, Springer International Publishing, Switzerland
2. Toei, M., Saum, R., and Forgac, M. (2010) Regulation and isoform function of the V-ATPases. *Biochemistry* **49,** 4715–4723 CrossRef Medline
3. Futai, M., Nakanishi-Matsui, M., Okamoto, H., Sekiya, M., and Nakamoto, R. K. (2012) Rotational catalysis in proton pumping ATPases: from *E. coli* F-ATPase to mammalian V-ATPase. *Biochim. Biophys. Acta* **1817,** 1711–1721 CrossRef Medline
4. Casey, J. R., Grinstein, S., and Orlowski, J. (2009) Sensors and regulators of intracellular pH. *Nat. Rev. Mol. Cell Biol.* **11,** 50–61 Medline
5. Beyenbach, K. W., and Wieczorek, H. (2006) The V-type H^+ ATPase: molecular structure and function, physiological roles and regulation. *J. Exp. Biol.* **209,** 577–589 CrossRef Medline
6. Breton, S., and Brown, D. (2013) Regulation of luminal acidification by the V-ATPase. *Physiology* **28,** 318–329 CrossRef Medline
7. Forgac, M. (2007) Vacuolar ATPases: Rotary proton pumps in physiology and pathophysiology. *Nat. Rev. Mol. Cell Biol.* **8,** 917–929 CrossRef Medline
8. Sun-Wada, G.-H., and Wada, Y. (2013) Vacuolar-type proton pump ATPases: acidification and pathological relationships. *Histol. Histopathol.* **28,** 805–815 Medline
9. Hinton, A., Bond, S., and Forgac, M. (2009) V-ATPase functions in normal and disease processes. *Pfluegers Arch.* **457,** 589–598 CrossRef
10. Ochotny, N., Van Vliet, A., Chan, N., Yao, Y., Morel, M., Kartner, N., von Schroeder, H. P., Heersche, J. N., and Manolson, M. F. (2006) Effects of human a3 and a4 mutations that result in osteopetrosis and distal renal tubular acidosis on yeast V-ATPase expression and activity. *J. Biol. Chem.* **281,** 26102–26111 CrossRef Medline
11. Kornak, U., Schulz, A., Friedrich, W., Uhlhaas, S., Kremens, B., Voit, T., Hasan, C., Bode, U., Jentsch, T. J., and Kubisch, C. (2000) Mutations in the a3 subunit of the vacuolar H^+-ATPase cause infantile malignant osteopetrosis. *Hum. Mol. Genet.* **9,** 2059–2063 CrossRef Medline
12. Kartner, N., Yao, Y., Bhargava, A., and Manolson, M. F. (2013) Topology, glycosylation and conformational changes in the membrane domain of the vacuolar H^+-ATPase *a* subunit. *J. Cell. Biochem.* **114,** 1474–1487 CrossRef Medline
13. Wagner, C. A., Finberg, K. E., Breton, S., Marshansky, V., Brown, D., and Geibel, J. P. (2004) Renal vacuolar H^+-ATPase. *Physiol. Rev.* **84,** 1263–1314 CrossRef Medline
14. Toyomura, T., Murata, Y., Yamamoto, A., Oka, T., Sun-Wada, G.-H., Wada, Y., and Futai, M. (2003) From lysosomes to the plasma membrane: localization of vacuolar-type H^+-ATPase with the a3 isoform during osteoclast differentiation. *J. Biol. Chem.* **278,** 22023–22030 CrossRef Medline
15. Bexiga, M. G., and Simpson, J. C. (2013) Human diseases associated with form and function of the Golgi complex. *Int. J. Mol. Sci.* **14,** 18670–18681 CrossRef Medline
16. Guillard, M., Dimopoulou, A., Fischer, B., Morava, E., Lefeber, D. J., Kornak, U., and Wevers, R. A. (2009) Vacuolar H^+-ATPase meets glycosylation in patients with cutis laxa. *Biochim. Biophys. Acta* **1792,** 903–914 CrossRef Medline
17. Fischer, B., Dimopoulou, A., Egerer, J., Gardeitchik, T., Kidd, A., Jost, D., Kayserili, H., Alanay, Y., Tantcheva-Poor, I., Mangold, E., Daumer-Haas, C., Phadke, S., Peirano, R. I., Heusel, J., Desphande, C., *et al.* (2012) Further characterization of *ATP6V0A2*-related autosomal recessive cutis laxa. *Hum. Genet.* **131,** 1761–1773 CrossRef Medline
18. Kornak, U., Reynders, E., Dimopoulou, A., van Reeuwijk, J., Fischer, B., Rajab, A., Budde, B., Nürnberg, P., Foulquier, F., ARCL Debre-type Study Group, Dobyns, W. B., Quelhas, D., Vilarinho, L., Leao-Telas, E., Greally, M., Seemanova, E., *et al.* (2008) Impaired glycosylation and cutis laxa caused by mutations in the vesicular H^+-ATPase subunit ATP6V0A2. *Nat. Genet.* **40,** 32–34 CrossRef Medline
19. Sobacchi, C., Schulz, A., Coxon, F. P., Villa, A., and Helfrich, M. H. (2013) Osteopetrosis: genetics, treatment and new insights into osteoclast function. *Nat. Rev. Endocrinol.* **9,** 522–536 CrossRef Medline
20. Bhargava, A., Voronov, I., Wang, Y., Glogauer, M., Kartner, N., and Manolson, M. F. (2012) Osteopetrosis mutation R444L causes ER retention and misprocessing of vacuolar H^+-ATPase *a3* subunit. *J. Biol. Chem.* **287,** 26829–26839 CrossRef Medline
21. Stover, E. H., Borthwick, K. J., Bavalia, C., Eady, N., Fritz, D. M., Rungroj, N., Giersch, A. B., Morton, C. C., Axon, P. R., Akil, I., Al-Sabban, E. A., Baguley, D. M., Bianca, S., Bakkaloglu, A., Bircan, Z., *et al.* (2002) Novel *ATP6V1B1* and *ATP6V0A4* mutations in autosomal recessive distal renal tubular acidosis with new evidence for hearing loss. *J. Med. Genet.* **39,** 796–803 CrossRef Medline
22. Batlle, D., and Haque, S. K. (2012) Genetic causes and mechanisms of distal renal tubular acidosis. *Nephrol. Dial. Transplant.* **27,** 3691–3704 CrossRef Medline
23. Schep, D. G., Zhao, J., and Rubinstein, J. L. (2016) Models for the a subunits of the *Thermus thermophilus* V/A-ATPase and *Saccharomyces cervisiae* V-ATPase enzymes by cryo-EM and evolutionary covariance. *Proc. Natl. Acad. Sci. U.S.A.* **113,** 3245–3250 CrossRef Medline
24. Mazhab-Jafari, M. T., Rohou, A., Schmidt, C., Bueler, S. A., Benlekbir, S., Robinson, C. V., and Rubinstein, J. L. (2016) Atomic model for the membrane-embedded V_o motor of a eukaryotic V-ATPase. *Nature* **359,** 118–122
25. Esmail, S., Yao, Y., Kartner, N., Li, J., Reithmeier, R. A., and Manolson, M. F. (2016) *N*-Linked glycosylation is required for vacuolar H^+-ATPase (V-ATPase) *a4* subunit stability, assembly, and cell surface expression. *J. Cell. Biochem.* **117,** 2757–2768 CrossRef Medline
26. Esmail, S., Kartner, N., Yao, Y., Kim, J. W., Reithmeier, R. A., and Manolson, M. F. (2018) *N*-Linked glycosylation of *a* subunit isoforms is critical for vertebrate vacuolar H^+-ATPase (V-ATPase) biosynthesis. *J. Cell. Biochem.* **119,** 861–875 CrossRef Medline
27. Maley, F., Trimble, R. B., Tarentino, A. L., and Plummer, T. H., Jr. (1989) Characterization of glycoproteins and their associated oligosaccharides through the use of endoglycosidases. *Anal. Biochem.* **180,** 195–204 CrossRef Medline
28. Freeze, H. H., and Kranz, C. (2010) Endoglycosidase and glycoamidase release of *N*-linked glycans. *Curr. Protoc. Mol. Biol.* **Chapter 12,** Unit 12.4
29. Ramachandran, N., Munteanu, I., Wang, P., Ruggieri, A., Rilstone, J. J., Israelian, N., Naranian, T., Paroutis, P., Guo, R., Ren, Z.-P., Nishino, I., Charbrol, B., Pellissier, J.-F., Minetti, C., Udd, B., *et al.* (2013) VMA21 deficiency prevents vacuolar ATPase assembly and causes autophagic vacuolar myopathy. *Acta Neuropathol. (Berl).* **125,** 439–457 CrossRef
30. Ryan, M., Graham, L. A., and Stevens, T. H. (2008) Voa1p functions in V-ATPase assembly in the yeast endoplasmic reticulum. *Mol. Biol. Cell* **19,** 5131–5142 CrossRef Medline
31. Hill, K., and Cooper, A. A. (2000) Degradation of unassembled Vph1p reveals novel aspects of the yeast ER quality control system. *EMBO J.* **19,** 550–561 CrossRef Medline
32. Toei, M., Toei, S., and Forgac, M. (2011) Definition of membrane topology and identification of residues important for transport in subunit a of the vacuolar ATPase. *J. Biol. Chem.* **286,** 35176–35186 CrossRef Medline
33. Lemus, L., and Goder, V. (2014) Regulation of endoplasmic reticulum-associated protein degradation (ERAD) by ubiquitin. *Cells* **3,** 824–847 CrossRef Medline
34. Hurtado-Lorenzo, A., Skinner, M., El Annan, J., Futai, M., Sun-Wada, G.-H., Bourgoin, S., Casanova, J., Wildeman, A., Bechoua, S., Ausiello, D. A., Brown, D., and Marshansky, V. (2006) V-ATPase interacts with

ARNO and Arf6 in early endosomes and regulates the protein degradative pathway. *Nat. Cell Biol.* **8,** 124–136 CrossRef Medline

35. Seol, J. H., Shevchenko, A., Shevchenko, A., and Deshaies, R. J. (2001) Skp1 forms multiple protein complexes, including RAVE, a regulator of V-ATPase assembly. *Nat. Cell Biol.* **3,** 384–391 CrossRef Medline
36. Kawasaki-Nishi, S., Nishi, T., and Forgac, M. (2001) Yeast V-ATPase complexes containing different isoforms of the 100-kDa a-subunit differ in coupling efficiency and *in vivo* dissociation. *J. Biol. Chem.* **276,** 17941–17948 CrossRef Medline
37. Malkus, P., Graham, L. A., Stevens, T. H., and Schekman, R. (2004) Role of Vma21p in assembly and transport of the yeast vacuolar ATPase. *Mol. Biol. Cell* **15,** 5075–5091 CrossRef Medline
38. Su, Y., Blake-Palmer, K. G., Sorrell, S., Javid, B., Bowers, K., Zhou, A., Chang, S. H., Qamar, S., and Karet, F. E. (2008) Human H^+ATPase a4 subunit mutations causing renal tubular acidosis reveal a role for interaction with phosphofructokinase-1. *Am. J. Physiol. Renal Physiol.* **295,** F950–F958 CrossRef Medline
39. Guevara-Coto, J., Schwartz, C. E., and Wang, L. (2014) Protein sector analysis for the clustering of disease-associated mutations. *BMC Genomics* **15,** S4 CrossRef Medline
40. Valastyan, J. S., and Lindquist, S. (2014) Mechanisms of protein-folding diseases at a glance. *Dis. Model. Mech.* **7,** 9–14 CrossRef Medline
41. Okiyoneda, T., Veit, G., Dekkers, J. F., Bagdany, M., Soya, N., Xu, H., Roldan, A., Verkman, A. S., Kurth, M., Simon, A., Hegedus, T., Beekman, J. M., and Lukacs, G. L. (2013) Mechanism-based corrector combination restores ΔF508-CFTR folding and function. *Nat. Chem. Biol.* **9,** 444–4454 CrossRef Medline
42. Cheng, S. H., Gregory, R. J., Marshall, J., Paul, S., Souza, D. W., White, G. A., O'Riordan, C. R., and Smith, A. E. (1990) Defective intracellular transport and processing of CFTR is the molecular basis of most cystic fibrosis. *Cell* **63,** 827–834 CrossRef Medline
43. Biasini, M., Bienert, S., Waterhouse, A., Arnold, K., Studer, G., Schmidt, T., Kiefer, F., Gallo Cassarino, T., Bertoni, M., Bordoli, L., and Schwede, T. (2014) SWISS-MODEL: modelling protein tertiary and quaternary structure using evolutionary information. *Nucleic Acids Res.* **42,** W252–W258 CrossRef Medline
44. Van Durme, J., Delgado, J., Stricher, F., Serrano, L., Schymkowitz, J., and Rousseau, F. (2011) A graphical interface for the FoldX forcefield. *Bioinformatics* **27,** 1711–1712 CrossRef Medline